



Influence of Dynamic and Static Interference on the Internal Flow and Vibration and Noise Characteristics of Marine Centrifugal Pump

Z. Cheng^{1,2}, Q. Ma^{1,3}, H. Liu^{1†}, L. Dong¹ and Q. Pan¹

¹ National Research Center of Pumps, Jiangsu University, Zhenjiang 212013, China

² School of Mechanical and Aerospace Engineering, Gyeongsang National University, Jinju 52828, Republic of Korea

³ School of Mechanical and Electrical Engineering, Chuzhou University, Chuzhou 239000, China

†Corresponding Author Email: liuhoulin@ujs.edu.cn

ABSTRACT

To improve the overall performance of marine centrifugal pumps (MCPs), their vibration and noise performances were optimized using the hydraulic design of the volute casing parameters considering a constant hydraulic performance at a specific speed of 66.7. Numerical simulations of the full flow field, vibration, and noise were conducted for each of five volute base circle diameters. The impact of dynamic and static disturbances on the flow and vibration and noise characteristics were investigated. These results provide some theoretical and technical support for the design and application of MCPs. The flow pattern inside the volute becomes more uniform as the D_3 increases, but the pressure pulsation decreases. The total vibration levels of the inlet flange, outlet flange, and pump base decreased by 8.3%, 7.9%, and 12.3% respectively. The sound pressure of the flow noise at each characteristic frequency showed a different degree of decreasing trend.

Article History

Received March 11, 2023

Revised June 9, 2023

Accepted June 13, 2023

Available online July 29, 2023

Keywords:

Marine centrifugal pump
Base circle diameter
Dynamic and static interference
Vibration and noise characteristics
Numerical simulation

1. INTRODUCTION

Marine centrifugal pumps (MCPs) are important auxiliary equipment of marine systems. Hence, their vibration and noise performances are crucial. The vibration and noise pollution generated by the operation of MCPs could affect the physical and mental health of the crew owing to the limited cabin space. It would also pose a threat to the concealment and safety of military vessels (Zhou et al., 2013; Guo et al., 2018). Therefore, it is essential to research the vibration and noise characteristics of MCPs to improve their overall comprehensive performance.

Several factors influence the vibration and noise of a MCP. In terms of the structural aspects, low assembly precision, component wear, and rotor misalignment, rotor imbalance will cause serious vibration and noise of the pump set (Spence et al., 2008; Kunz & Nwekirk, 2009). However, the influence of these factors could be mitigated by improving the machining production. The hydraulic parameters are the key factors of fluid-induced vibration noise (Spence & Amaral-Teixeira, 2009). Scientists have investigated the effects of gap between the impeller and the volute on dynamic and static interference through several methods, such as adjusting the diameter of the

impeller (Mohamed et al., 2019), impeller inclination (Kuang et al., 2021), base circle diameter (Chan et al., 2007) and the setting angle of the tongue (Dong & Dou, 2021). However, the impeller is the main rotating power component, and its parameter adjustment could have a considerable impact on the external characteristics of the pump. Conversely, the base circle diameter and tongue setting angle have little influence on the external characteristics, which is notable for the qualitative study of the effect of dynamic and static interference on the vibration and noise of the pump (Iversen et al., 1960; Dong et al., 2018).

In 1989, Arndt et al. (1989) at the California Institute of Technology conducted the first experimental study of the pressure pulsation on the shroud of a centrifugal pump with or without a guide vane. They observed that the dynamic and static interference intensified the pressure pulsation on the impeller shroud. Chu et al. (1995) plotted a pressure distribution map based on particle displacement velocimetry (PDV) data, identified the main noise sources of centrifugal pumps by combining the noise and pressure measurements, and considered that the dynamic and static interference mainly induced the blade frequency pulsation. Ma et al. (2021) studied the vibration characteristics of compressor impellers and determined

NOMENCLATURE			
b_2	outlet width	n	speed
b_3	inlet width	P	shaft power
D_1	inlet diameter	Q_d	flow rate
D_2	outlet diameter	z	number of blades
D_3	base circle diameter	φ_0	tongue setting angle
D_d	outlet diameter	φ	blade wrap angle
H	head	η	pump efficiency
L_v	vibration velocity level		

the resonance state of the impeller via modal analysis. The main vibration of the impeller during resonance is the vibration component of the fundamental frequency and the resonance frequency, and the vibration amplitude is larger under the resonance frequency. Shadab et al. (2022) studied the hydraulic performance of centrifugal pumps by increasing the clearance between the impeller and the casing. The results showed that trimming the shroud reduces the performance of the design point, and the shroud-trimmed impeller has a larger radial force than the closed impeller owing to the lack of uniform pressure distribution around the impeller outlet. Jia et al. (2022) studied the impact of closed, semi-open, and open impellers on the running stability of pumps and showed that the pressure stability at the tongue of the closed impeller is the best, but that of the open impeller is the worst owing to the dynamic and static interaction. The closed impeller has the lowest shroud vibration, followed by the semi-open impeller, and the open impeller has the highest vibration.

Owing to the limitations of the test, it is difficult to acquire the characteristics of the fluid excitation force, and the complex flow structure generated by the interaction between the impeller and the volute or guide vane only by the test alone. For this reason, scholars have studied the hydraulic excitation characteristics of pumps and the vibration and noise characteristics of rotating machinery via numerical simulations. As early as 1996, Croba & Kueny (1996) from the Grenoble Research Centre in France numerically calculated the interference between the stator and rotor of centrifugal pumps based on the two-dimensional URANS equation. Yuan et al. (2009) studied the transient characteristics in a pump based on the $k-\epsilon$ turbulence model. The results showed that the frequency of pressure is consistent with the passing frequency of the blade, and the peak value of the pressure increases with increasing impeller radius. Atif et al. (2011) used the SST $k-\omega$ turbulence model to simulate the dynamic and static interference between the impeller and the guide vane, and between the impeller and the volute. They observed that the unsteady flow between the impeller and the guide vane affects the vibration and noise level of the pump. Based on the SST $k-\omega$ turbulence model, Chalghoum et al. (2018) simulated the unsteady flow of a pump, and indicated that the unsteady action of the pump is mainly related to the radial force of the impeller, and that the dynamic and static interference is the main excitation source of vibration and liquid-borne noise. In addition, the pressure and excitation force characteristics between the fixed element and rotor of the centrifugal pump were analyzed. The results showed that the pressure amplitude is the minimum at

$1.0Q_d$, and the pressure amplitude at the tongue of the volute is larger than that at other parts. Ren et al. (2022) studied the noise of centrifugal fans with an eccentric impeller by using the mixed method of separated eddy simulation and finite element method (FEM). The characteristics of the noise spectrum and sound directivity change significantly, the rotational frequency caused by the impeller eccentricity increases, and the total sound pressure level (SPL) increases with increasing eccentricity.

Thus, studies on the dynamic and static interference of centrifugal pumps mainly focus on the analysis of the internal flow characteristics of the centrifugal pump, such as energy performance, pressure pulsation, and radial force. Some scholars have also studied the influence of dynamic and static clearance on fluid-induced vibration based on different research objects. In this study, considering an unchanged hydraulic performance, both numerical calculations and experiments were conducted to research the vibration and noise performances of a MCP under the influence of dynamic and static disturbance, to provide reference for the design of MCPs.

2. NUMERICAL CALCULATION MODEL

2.1 Establishment of Fluid Domain Model

An MCP with a specific speed of 66.7 was selected as the research object, and its parameters were as follows: flow $Q_d=25 \text{ m}^3/\text{h}$, head $H=35 \text{ m}$, and rotational speed $n=2950 \text{ r/min}$. The geometrical parameters of the overcurrent components of the MCP are listed in Table 1.

The fluid calculation domain of the overall flow field consists of the inlet elbow, impeller water body, cavity, volute water body, and outlet extension. To develop the fluid at the inlet of the MCP fully and achieve a stable state, an inlet extension of four times the pipe diameter was installed before the inlet elbow. The computational model of the full flow field is shown in Fig. 1.

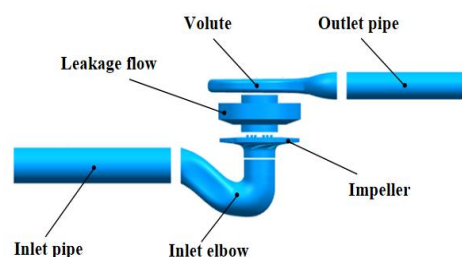


Fig. 1 Calculation model of the full flow field of a MCP

Table 1 Geometric parameters of the flow passage components

Flow passage components	Geometric parameters	Symbol	Value
Impeller	Inlet diameter/mm	D_1	65
	Outlet diameter/mm	D_2	165
	Outlet width/mm	b_2	7
	Blade wrap angle/ $^\circ$	φ	110
	Number of blades	z	6
Volute	Base circle diameter/mm	D_3	176
	Tongue setting angle/ $^\circ$	φ_0	23
	Inlet width/mm	b_3	20
	Outlet diameter/mm	D_d	50

Table 2 Grid independence verification

Scheme	Grid number	Node number	Head /m
01	1647157	1474148	34.5
02	2457849	2287414	35.2
03	2914979	2741943	35.5
04	3278458	3024785	35.5
05	3715756	3546854	35.6

as the standard.

As the fluid-induced vibration noise mainly focuses on the flow information of the fluid domain wall and has certain requirements for the mesh. The key parts such as the impeller blades and volute tongue are locally refined during the meshing process. Ultimately, the y^+ value of the MCP wall is guaranteed to meet the requirements (Cao et al., 2022).

2.2 Establishment of Structural Domain Model

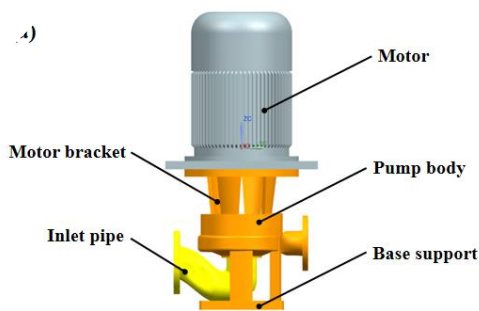
The MCP unit system consists of a motor, bracket, pump body, water inlet pipe, base, and rotor. The 3D structure model of the system is shown in Fig. 2.

ANSYS 18.0 Workbench finite element software was applied to construct the finite element analysis model of the MCP unit. The Solid 187 unit was used for both the rotor and the casing, and the Surf 154 unit was used for the structural surface where flow and electromagnetic fields are in contact, as shown in Fig. 3. The external structure model is built by simplifying the details that have less influence on the structure, to make the external structure mesh more ideal, improve the calculation accuracy, and reduce the calculation time. When building the rotor model, it is necessary to analyze the bearing position stress, and hence, the shaft part is cut and simplified, and the shaft part mesh is an all-hexahedral mesh and is coded.

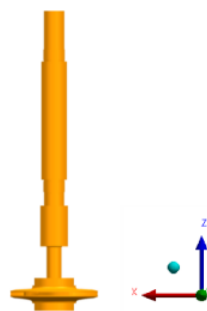
2.3 Calculation Settings

2.3.1 Flow Field Calculation Settings

The flow field is calculated using the CFX full flow field numerical simulation method. The inlet is set to hydrostatic conditions, and the outlet is set to the velocity outlet. The medium is clear water at 25 °C, the relative pressure is set to 0 for the entire calculation, and the turbulence model is the SST $k-\omega$ model. The wall surface is set to a no-slip wall surface, and the roughness is set to 12.5 μm . The dynamic-static domain intersection mode is “frozen rotor”, and the intersection between each static domain is set to static/static intersection. The calculation convergence accuracy is set to 10^{-5} , and the numerical solution format is the second-order high-precision format. The non-constant calculation parameters are set based on the constant results, and the dynamic and static intersection interface is set to transient rotor-stator, and the pitch angle is set to 360° to ensure the transient effect of the impeller calculation domain. The time step is set to 0.565e-4s, i.e., every 1° of the impeller rotation is one time



(a)



(b)

Fig. 2 3D structural model of the MCP unit (a) external structure, (b) rotor system

The meshing of the calculation model was completed based on ICFM-CFD. In the finite element calculation, the mesh quality is the key to the accuracy of the calculation results, to account for the small error of the calculation results and avoid wasting resources in the calculation of the kernel. The results of the mesh independence verification are listed in Table2. The third scheme is selected for the calculation with a head deviation within 1%

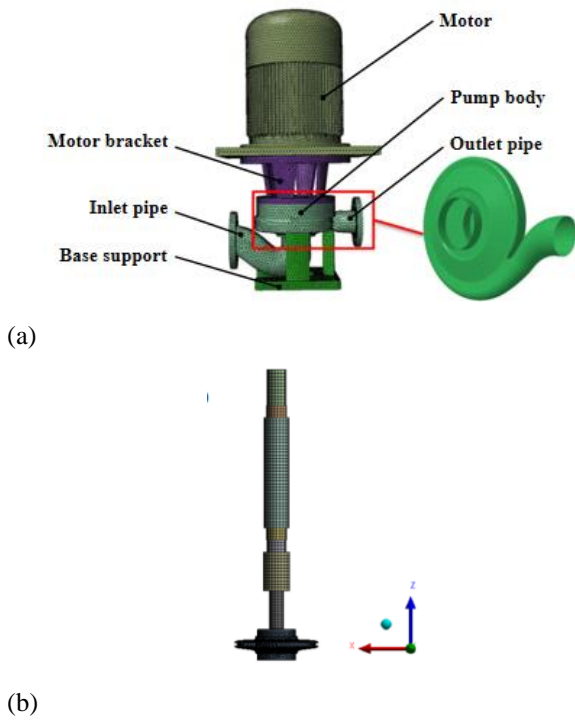


Fig. 3 Finite element model of the MCP unit
(a) external structure, (b) rotor system

step. When the flow field is stabilized, the pressure information on the impeller surface and the casing is extracted. The extracted pressure information is used as the excitation source to continue the calculation, and the total time is set to 0.25 s.

2.3.2 Vibration Noise Calculation Settings

Figure 4 shows the calculation method and flow of the vibration and noise of the MCP. The specific process is as follows: (1) The unsteady flow is calculated for the water model of the MCP, and the pressure pulsation on the wall of the MCP model, the radial force of the impeller, and the rotating dipole sound source are obtained. (2) The finite element model of the MCP group structure is established to solve the modal response of the structure. (3) The fluid excitation vibration is calculated based on the pressure pulsation excitation and shaft vibration transmission. (4) The acoustic boundary element method (BEM) model of the MCP internal field is established, and the flow noise is calculated based on the processing results of the pressure pulsation and impeller excitation sound source. (5) When calculating the vibration of the MCP, the modal superposition method is used to calculate the vibration characteristics based on the modal response results and step (3). (6) When calculating the internal field noise of the MCP, the acousto-vibration method is applied to calculate the fluid-induced noise based on the modal response and step (4).

2.4 Research Scheme

Dynamic and static interference is the primary influence impacting the flow-induced vibration noise of the MCP. Considering an unchanged hydraulic performance, the hydraulic design of the D_3 is carried out to explore the impact of the dynamic and static interference on the vibration noise of the MCP. Based on the original model $D_3=176$ mm, D_3 is selected as a scheme of 168 mm, 171 mm, 181 mm, and 186 mm, and the hydraulic design software PCAD is used to design the hydraulic parameters. Figure 5 shows the 2D hydraulic models of different research schemes.

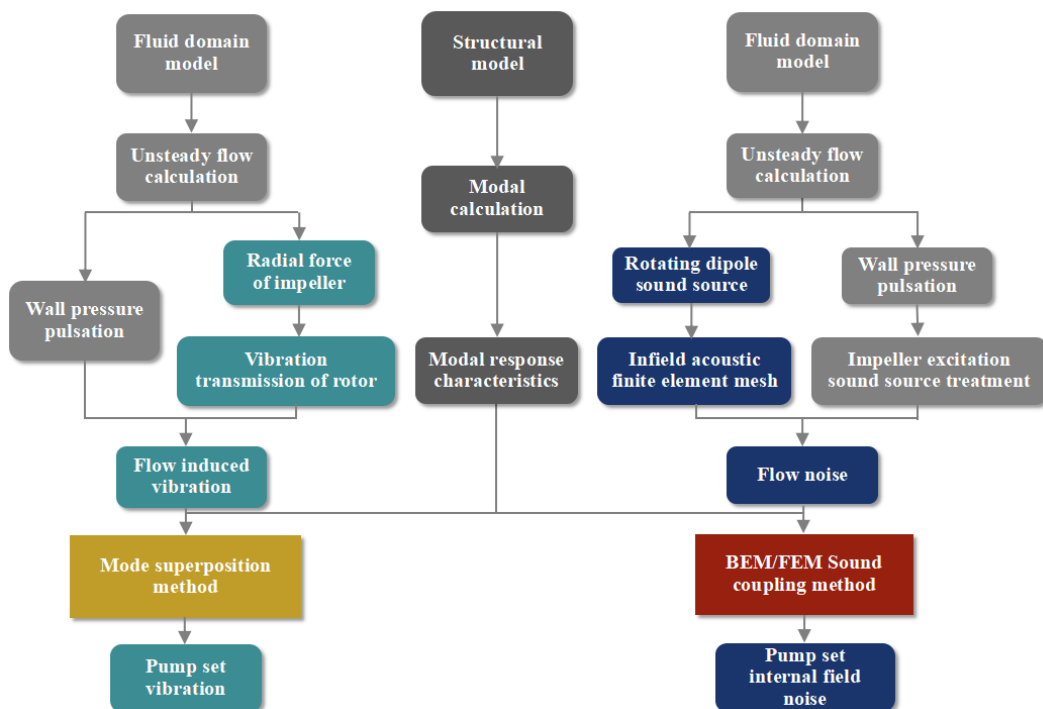


Fig. 4 Vibration and noise calculation process of the MCP

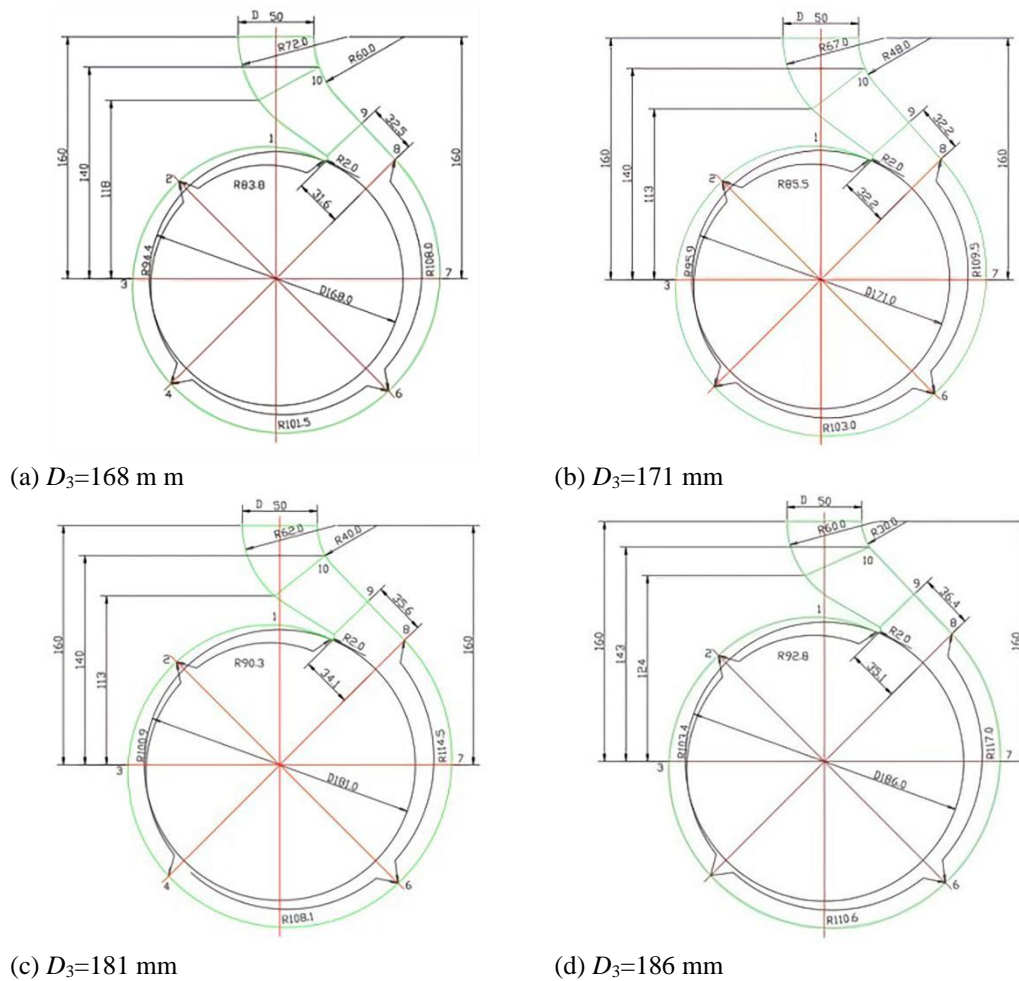


Fig. 5 2D hydraulic models of different research schemes

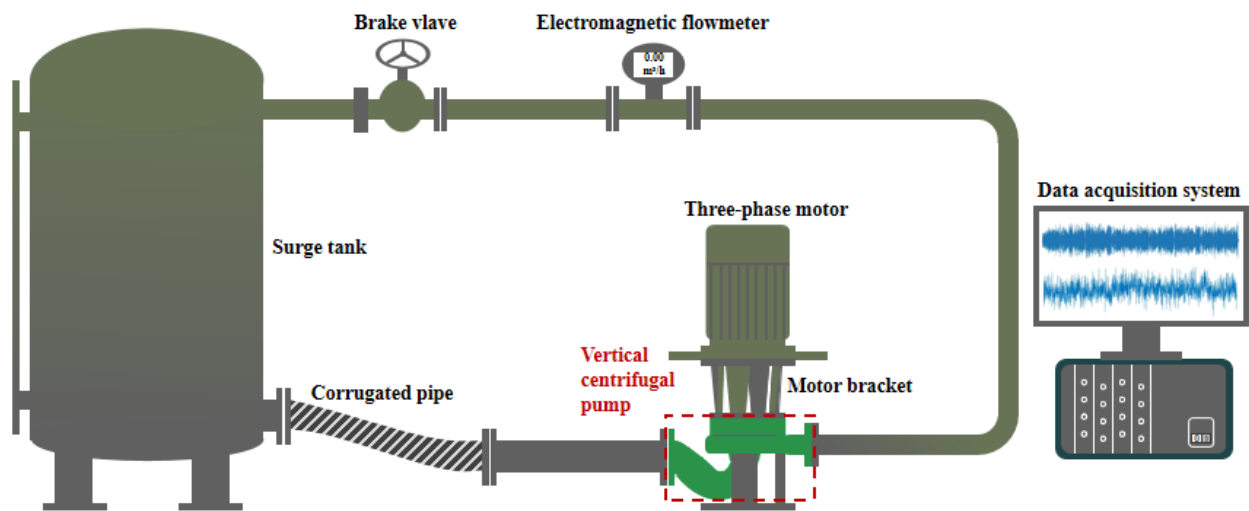


Fig. 6 Schematic diagram of the MCP closed test system

3. TEST DEVICE AND RESULTS

3.1 Closed Test Bed System

The enclosed MCP test stand consists of a MCP unit, pressure regulator tank, pipeline system, and data acquisition system. Figure 6 shows a schematic of the test rig system. The energy characteristic parameters of the

MCP are collected using an electromagnetic flowmeter, a pressure transmitter, and voltage and current transformers. The vibration parameters are acquired using an INV9832 vibration acceleration sensor. The liquid load noise is detected using an RHSA-10 hydrophone. The location of measurement points for the system vibration and liquid-borne noise is shown in Fig. 7. Table 3 presents the parameter configurations of different sensors.

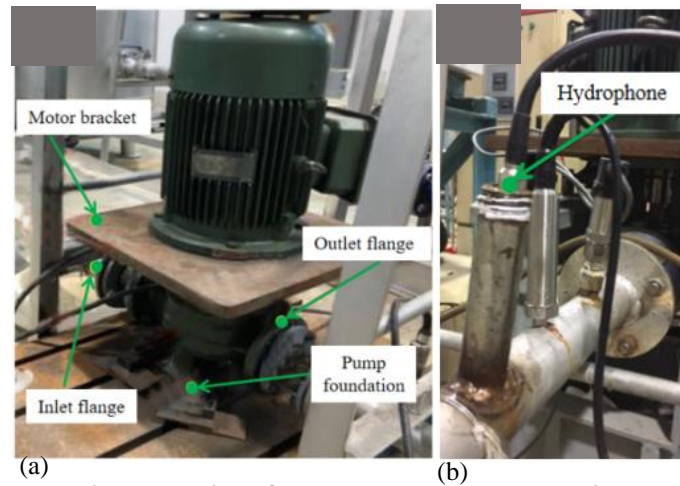


Fig. 7 Location of the sensor measurement points
 (a) vibration acceleration sensor, (b) liquid load noise sensor

Table 3 Parameter configurations of various sensors

Sensor type	Signal type	Measuring range	Accuracy class
Electromagnetic flowmeter	Pump flow/ m ³ /h	0~50 m ³ /h	±0.25%
Inlet pressure transmitter	Pump inlet pressure/ kPa	-100~100 kPa	±0.1%
Outlet pressure transmitter	Pump inlet pressure/ kPa	0~1000 kPa	±0.1%
Voltage transformer	Pump shaft power/ kW	0~500 V	Grade 0.2
Current transformer		0~10 A	Grade 0.1
Vibration acceleration sensor	Vibration acceleration of pump inlet flange/ g	-50~50 g	±3%
	Vibration acceleration of pump outlet flange/ g		
	Vibration acceleration of pump seat/ g		
Hydrophone	Liquid load noise of pump outlet/ dB	<i>f</i> :1~200 kHz	-

3.2 Comparison of Results

The formulae for the head H and pump efficiency η (Liu et al., 2020) of the clear water test are:

$$H = \frac{P_o - P_1}{\rho g} + \frac{V_o^2 - V_1^2}{2g} + (Z_o - Z_1) \quad (1)$$

$$\eta = \frac{\rho g Q H}{P} \quad (2)$$

where, $P_o - P_1$, $V_o^2 - V_1^2$, and $Z_o - Z_1$ represent the differences in the pressure, velocity, and potential energy, respectively. P is the shaft power (W), and Q is the flow rate (m³/s).

The speed of pumps is generally used to measure the level of vibration fluctuation. The vibration velocity level is used to reflect the average energy of the vibration (Cheng et al., 2022). The vibration level of different measurement points can be intuitively compared. The formula is as follows:

$$L_v = 20 \log_{10} \frac{v_{rms}}{v_0} \quad (3)$$

where: v_{rms} is the vibration velocity value; v_0 is the reference value, which is 1×10^{-9} m/s. v in Eq. (3) is the

vibration velocity level over the entire time, which is called the total vibration level.

The combined uncertainty E of the system is a parameter that measures the accuracy of the results of the system, which mainly consists of the random uncertainty E_R and the system uncertainty E_s . The confidence coefficient in the confidence interval was considered to be 95%.

The comparison data of the numerical calculations and test results of the energy characteristics of the MCP is shown in Fig. 8. The maximum errors of the calculation of the head and MCP efficiency are 3.95% and 2.82%, respectively, under $0.6Q_d \sim 1.4Q_d$. It is clear that the numerical simulation method is feasible and the calculation results can provide a more accurate load for the vibration and noise calculations of the MCP.

By analyzing and comparing the numerical calculations and test results of at the three vibration measurement points and the internal field noise of the MCP in Fig. 9, it is observed that the characteristic frequencies of the vibration velocity level in Fig. 9(a)~(c) are consistent with each other at the axial pass frequency

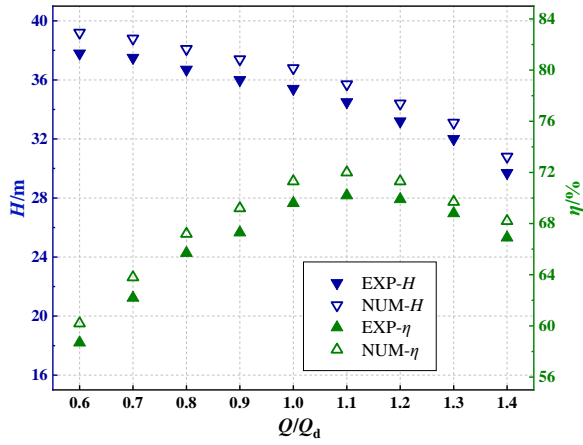


Fig. 8 Performance comparison of the numerical calculations and experimental tests

($1f_{APF}$) and blade pass frequency ($1f_{BPF}$). The main frequencies are $1f_{BPF}$, and the other characteristic frequency signals have a certain correspondence. The sound pressure level (SPL) of the noise in Fig. 9(d) is consistent with the characteristic frequencies at $1f_{BPF}$ and its frequency multiplier.

Table 4 lists the comparison results of the experimental and simulated values at the characteristic frequencies for each measurement point. The maximum rate of change of the vibration velocity level at $1f_{APF}$ at the three vibration measurement points is -7.3%, whereas the maximum rate of change at $1f_{BPF}$ is -1.7%. The rate of change of the SPL for the internal field noise at $1f_{BPF}$ and $2f_{BPF}$ is less than -1%. The numerical calculation method is feasible and can be better applied to study the vibration and noise characteristics of the MCP.

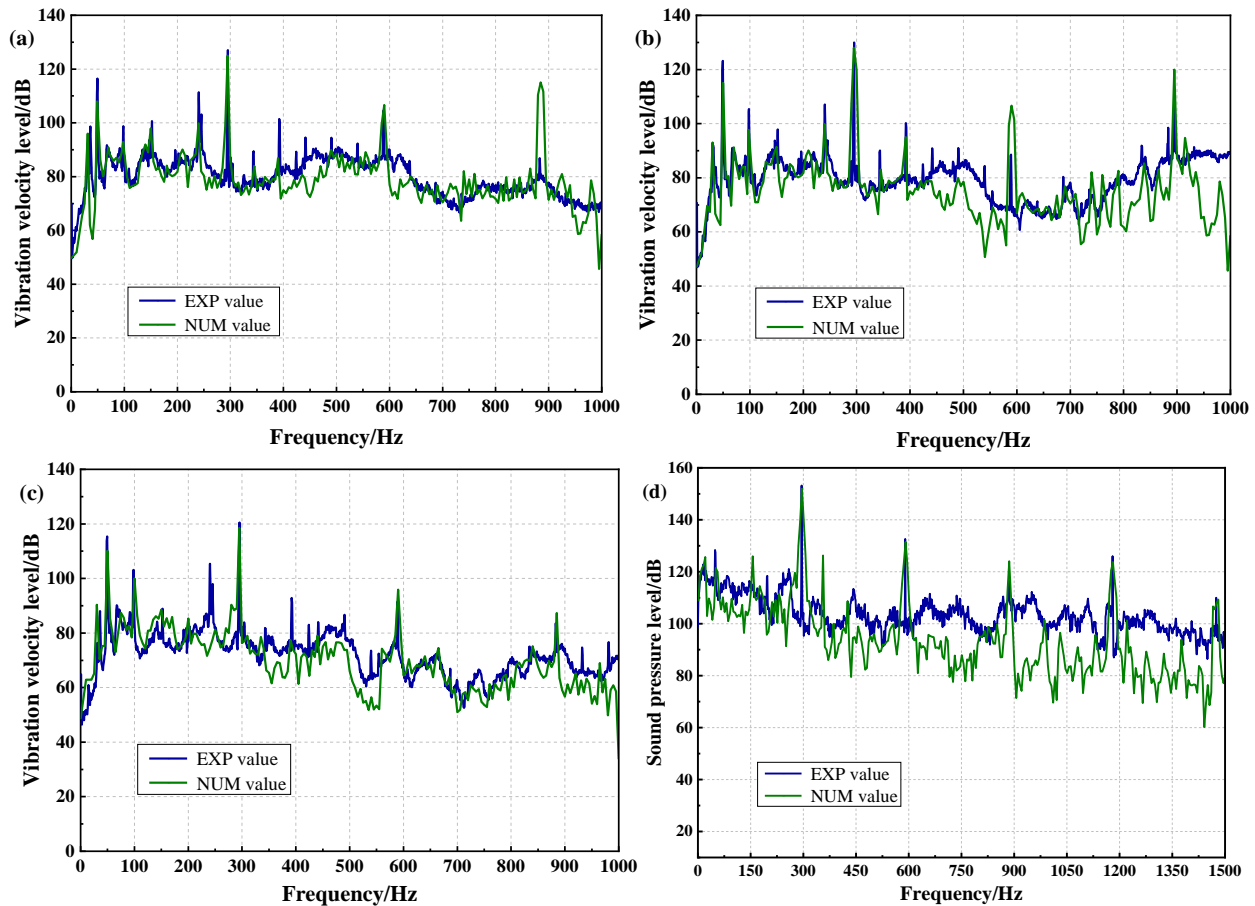


Fig. 9 Comparison of the numerical calculations and test results of the MCP vibration noise

(a) MCP outlet flange, (b) MCP inlet flange, (c) MCP base, (d) MCP outlet

Table 4 Numerical simulation and test results of the error of vibration and noise at each measurement point.

Type	Vibration velocity level/dB						Sound pressure level/dB		
	Inlet flange		Outlet flange		MCP base		MCP outlet		
	$1f_{APF}$	$1f_{BPF}$	$1f_{APF}$	$1f_{BPF}$	$1f_{APF}$	$1f_{BPF}$	$1f_{BPF}$	$2f_{BPF}$	$3f_{BPF}$
EXP	116.5	127	123.2	130	115.4	120.5	153.2	132.6	116.5
NUM	108	125	115	128	110.1	118.5	152	131.5	124
Change rate/%	-7.3	-1.6	-6.7	-1.5	-4.6	-1.7	-0.8	-0.8	6.4

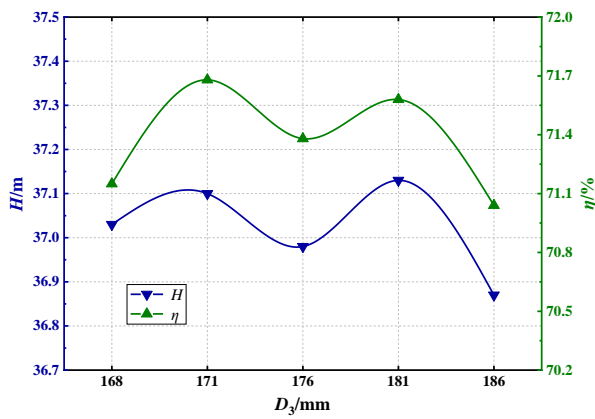


Fig. 10 Results of the external characteristics for different base circle diameters

4. NUMERICAL SIMULATION RESULTS AND ANALYSIS

4.1 External Characteristics and Internal Flow Characteristics

Figure 10 shows the energy characteristic results of the volutes with different base circle diameters of the MCP calculated under the full flow field. Compared with the original model, an appropriate change of the volute D_3 changes the MCP head and efficiency, and there is an optimum value of the D_3 that makes the MCP head and efficiency reach their optimum values. If the D_3 is changed by more than 5%, the head and efficiency will decrease. In this research scheme, the change rate of the head is not more than 0.2%, and the change rate of the efficiency is not more than 0.9%. The comprehensive performance variation rule of the MCP is studied under the condition that the external characteristic results are unchanged, which shows the rationality of the design scheme.

The internal flow pattern of fluid excitation can be fully understood by analyzing the velocity distribution cloud and cross-sectional pressure and flow distribution diagrams, as shown in Fig. 11 and Fig. 12.

Firstly, as the D_3 increases, the velocity of the working surface of the blade passing the tongue in the impeller basin changes significantly, especially at the tail of the blade. No significant changes were found in the velocities of other areas of the impeller. Observation of the basin in the red circle at the same position reveals that the fluid velocity gradient at the blade working surface decreases as D_3 increases when flowing through the tongue. When D_3 is less than 171 mm, the fluid velocity gradient in this region is significantly larger than the velocity gradient in the other blade working surfaces., & the velocity gradient is similar when D_3 is greater than 171 mm. The variation pattern of the velocity gradient is further reflected in the flow distribution in the blue box of Fig. 12. When D_3 is less than 171 mm, the region of dynamic-static junction shows obvious large vortex flow. As the D_3 increases, the vortex in this region gradually disappears and the streamline distribution becomes more and more smooth.

Secondly, when D_3 is less than 171 mm, there is a high speed area in the volute after the fluid flows out of the blade,

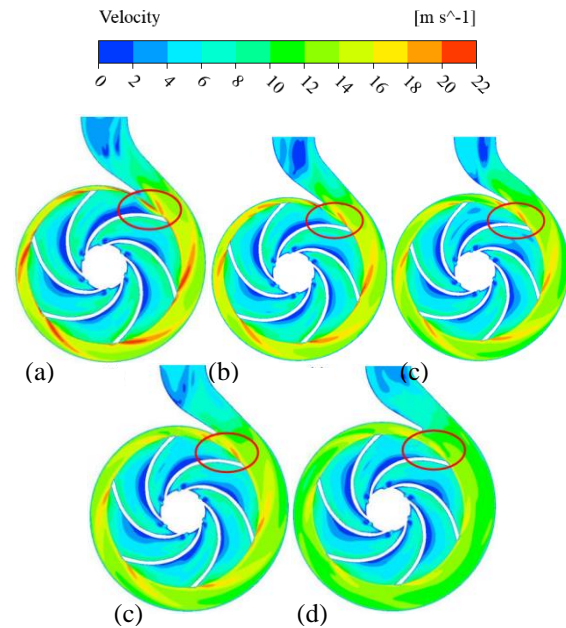


Fig. 11 Cloud image of velocity distribution in the middle section of the volute with different base circle diameters

(a) $D_3=168$ mm, (b) $D_3=171$ mm, (c) $D_3=176$ mm, (d) $D_3=181$ mm, (e) $D_3=186$ mm

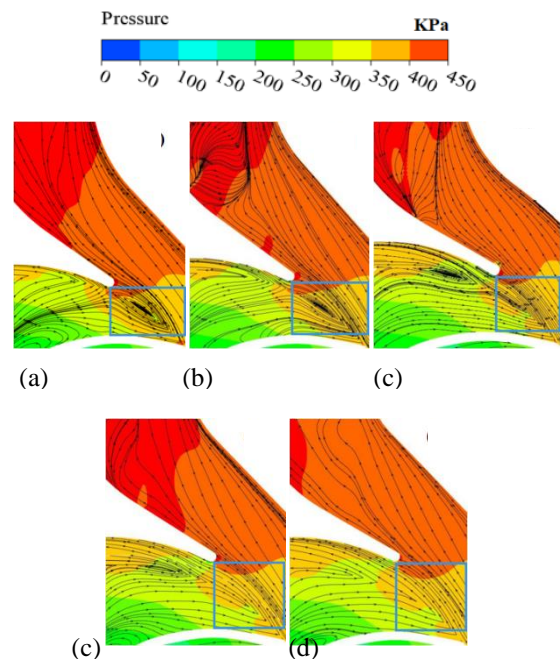


Fig. 12 Pressure and streamline distribution for different base circle diameters

(a) $D_3=168$ mm, (b) $D_3=171$ mm, (c) $D_3=176$ mm, (d) $D_3=181$ mm, (e) $D_3=186$ mm

and the overall velocity exceeds 12 m/s. As D_3 continues to increase, the flow velocity at the end of the blade in the volute continues to decrease, and the velocity gradient gradually decreases. The increase of D_3 causes the distance from the impeller outlet to the volute wall to increase, while the work done by the impeller remains unchanged. This makes the fluid

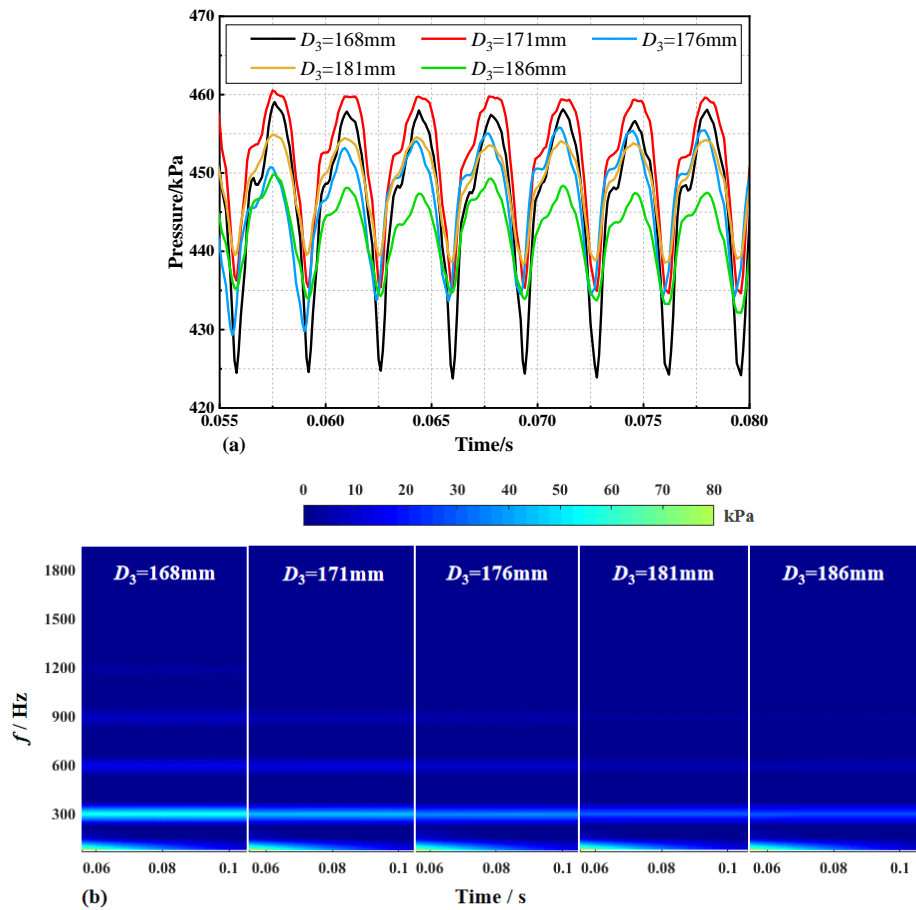


Fig. 13 Pressure pulsation distribution diagram of the MCP outlet

for different base circle diameters (a) time-domain figure, (b) continuous wavelet time-frequency diagram

flow out of the impeller increases the degree of diffusion, which eventually leads to a decrease in the velocity gradient. Due to the gradual reduction of the velocity gradient of the fluid in the volute, the vortex at the pump outlet gradually disappears and the downstream flow line becomes more stable and smooth. This law is also reflected in the pump outlet pressure pulsation data in Fig. 13. The pressure fluctuation gradually decreases as D_3 increases.

The analysis of the internal flow law, which is dominated by the dynamic-static interference region and developed towards the downstream region, is a prerequisite. Because the internal flow under the action of dynamic-static interference is one of the main excitation sources that cause the external characteristics of the MCP. The pressure pulsation as a combined manifestation of the internal flow variation is also the main parameter triggering the external characteristics for further analysis. The time-domain diagram and continuous wavelet time-frequency diagram of the pressure pulsation at the MCP outlet pipe for different base circle diameters is shown as Fig. 13. As the D_3 increases, the pressure shows a downward trend. When the D_3 is 171 mm, the outlet pressure pulsation reaches the maximum value, which is 460 kPa. When the D_3 is 168 mm, the outlet pressure fluctuation range is the largest, which is approximately 30 kPa. Figure 13(a) shows that the pressure at the outlet of the volute shows evident periodic changes for different

base circle diameters, which is an important reason for the forced vibration of the MCP body. According to Fig. 13(b), the main frequencies of the pressure at the outlet for different base circle diameters are all located at $1/f_{BPF}$, and the harmonic frequencies are distributed at the multipliers of $1/f_{BPF}$. As the D_3 increases, the amplitude of the main frequency and harmonic frequency gradually decreases. This indicates that the characteristic frequency of the fluid excitation does not change with the change in the D_3 , but the amplitude of each characteristic frequency shows a decreasing trend with increasing D_3 .

4.2 Vibration and Noise Characteristics

The natural frequency distribution of MCP units for the first 1000 Hz for different base circle diameters is shown in Fig. 14. Compared with the original model, changing the D_3 has no effect on the modal order of the MCP group, but has some effect on the natural frequency of each order. The natural frequencies of different schemes in the first four orders are the same, varying by approximately 1 Hz. The natural frequency varies considerably from the fifth order to the seventh order, particularly in the sixth order mode. When the base circle diameters are 168 mm, 171 mm, 176mm, and 181 mm, the sixth-order natural frequencies are 297 Hz, 291 Hz, 282 Hz, and 272 Hz, respectively. $D_3=186\text{mm}$ and a natural frequency of 263 Hz are considered for the solution. Thus, as the D_3 increases, the natural frequency of each mode advances at different rates.

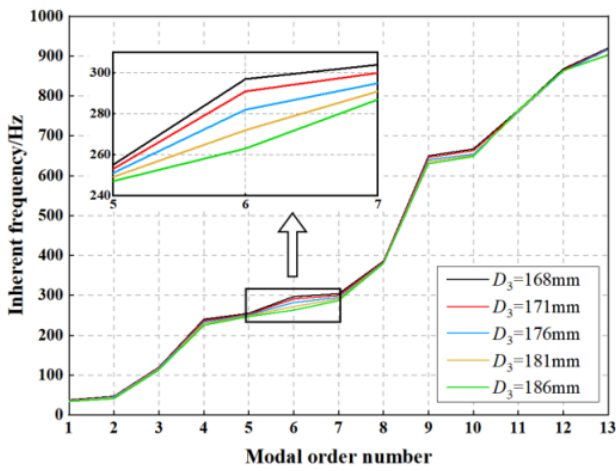


Fig. 14 Natural frequency distribution of the MCP unit at the first 1000Hz for different base circle diameters

The broadband vibration velocity spectra at each measurement point for different volute base circle diameters are obtained using the modal superposition method. Figures 15(a)~(c) show the broadband vibration velocity level spectral at each measurement point for different base circle diameters. Figure 15(a) shows that the main frequency of the vibration velocity level of the MCP inlet flange is at $1f_{BPF}$, and the harmonic frequency is at $2f_{BPF}$ and $1f_{APF}$. When $D_3=168$ mm, the characteristic frequency with a higher vibration velocity level appears in the vicinity of $3f_{BPF}$. As D_3 gradually increases, the amplitude at $1f_{APF}$ does not change significantly, the amplitudes at $1f_{BPF}$, $2f_{BPF}$ and $3f_{BPF}$ decrease to different degrees, and the energy amplitude of the vibration velocity level at $3f_{BPF}$ gradually decreases. Figure 15(b) shows the vibration velocity level of the MCP outlet flange. In general, the energy amplitude is larger than that of the MCP inlet flange, and there is a similar fluctuation rule. However, when D_3 is 168 mm and 171 mm, there is an apparent harmonic frequency near $1f_{BPF}$. With the gradual increase in D_3 , the energy amplitude at the harmonic frequency gradually decreases. This law is consistent with the flow pressure distribution and streamline distribution. Figure 15(c) shows the energy amplitude of the vibration velocity level of the MCP base, and the main vibration frequency is at $1f_{BPF}$. When D_3 is 168 mm and 171 mm, the energy amplitude at $1f_{BPF}$ is large, and there is an apparent harmonic frequency near $1f_{BPF}$. When D_3 increases to 176mm, the harmonic energy amplitude near $1f_{BPF}$ decreases. As D_3 continues to increase, the energy amplitude of $1f_{BPF}$ decreases to varying degrees.

The internal flow of the MCP is complex. With the change of D_3 , there are different degrees of dynamic-static interference, backflow and flow separation and other unstable flow phenomena. These unstable flows lead to pressure pulsation at the wall, inducing pump body vibration and noise generation. Combined with the results of the analysis of the internal flow law, it is not difficult to find the resonant frequency of the vibration velocity level at each measurement point near the characteristic frequency and the presence of large vortices near the

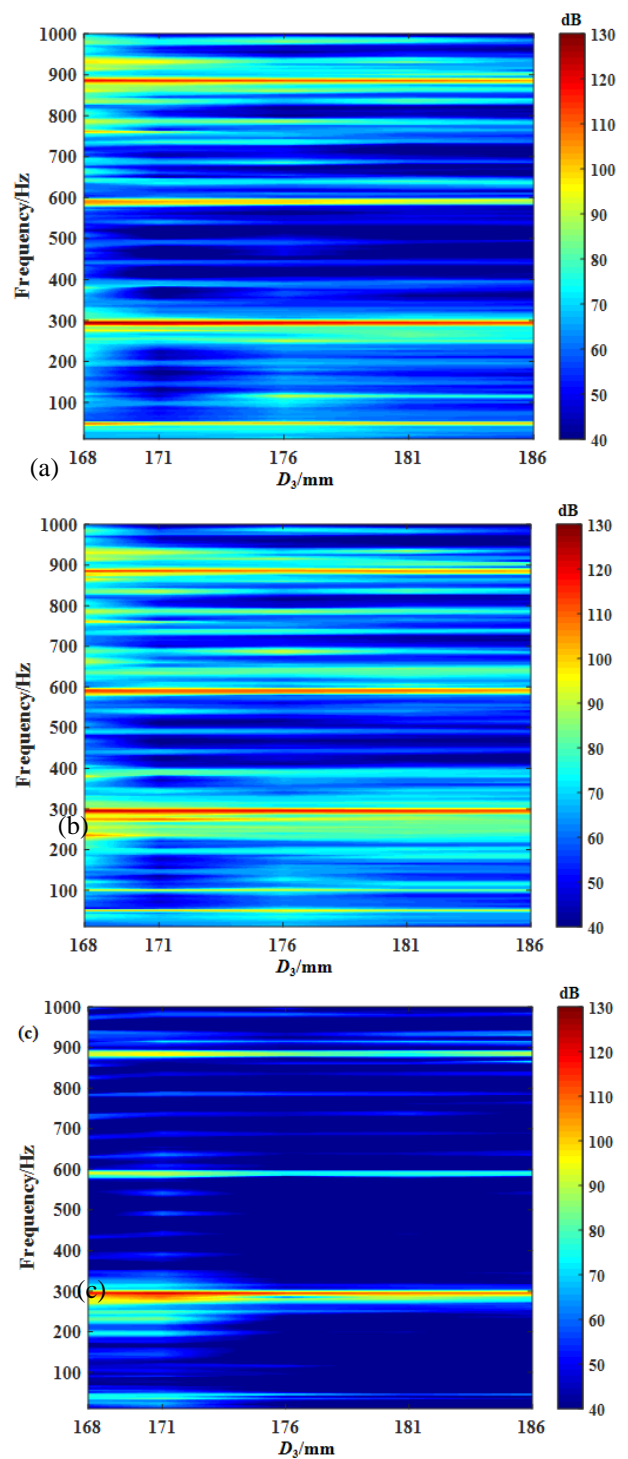


Fig. 15 Broadband vibration velocity level spectra at each measurement point for different base circle diameters (a) MCP outlet flange, (b) MCP inlet flange, (c) MCP base

tongue, the larger velocity gradient in the volute and downstream reflux phenomenon is closely related. Therefore, when D_3 is less than 171 mm, it is more likely to cause unstable flow phenomena and induce the vibration of the MCP.

The total vibration level was introduced to characterize the vibration for different base circle diameters to show the vibration change rule of the MCP body more clearly.

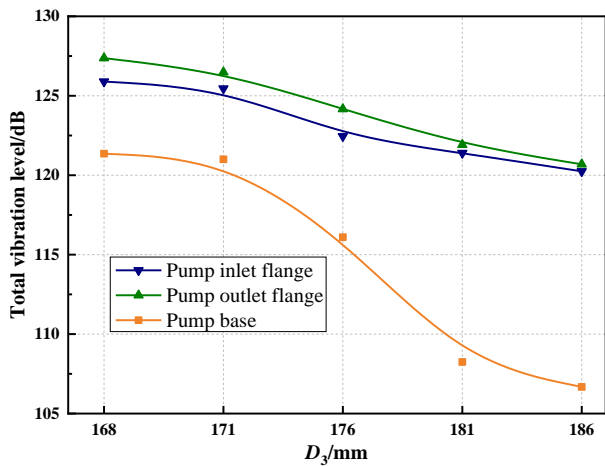


Fig. 16 Total vibration level at each measurement point for different base circle diameter.

Figure 16 shows the linear fitting results of the total vibration levels at each measurement point for different base circle diameters. The change in the D_3 has no effect on the order of the total vibration level at each measurement point. The order of the total vibration level at each point is: outlet flange > inlet flange > body base. As the D_3 increases, the total vibration level at each point decreases. The decay law and amplitude of the flanges are the same, and the total vibration level of the MCP base decreases further with increasing D_3 . When D_3 is increased from 168 mm to 186 mm, the total vibration levels at the measurement points of the MCP outlet flange, inlet flange, and base decreases by 7.9%, 8.3%, and 12.3%, respectively. The results show that the change in the D_3 has the greatest influence on the vibration of the MCP base.

For MCPs, the sound pressure spectrum law for the internal field noise at the inlet and outlet is the same, and the internal flow noise is propagated downstream, and hence, the internal field noise at the MCP outlet is greater than that at the inlet. The broadband spectrum of the flow noise at the outlet for different base circle diameters is shown in Fig. 17. As the D_3 changes, the frequencies in the sound pressure spectrum at the outlet do not change. The frequency is $1f_{BPF}$, and the characteristic frequency is distributed to $2f_{BPF}$, $3f_{BPF}$, $4f_{BPF}$, $5f_{BPF}$, and $6f_{BPF}$. With the increase in D_3 , the spectral law changes in the overall frequency band, and the amplitude of the SPL shows an overall decreasing tendency. The SPL of the flow noise for different base circle diameters is extracted and compared at each characteristic frequency as shown in Fig. 18. When D_3 is increased from 168 mm to 186 mm, the SPL of the $1f_{BPF}$, $2f_{BPF}$, and $3f_{BPF}$ decreases by 5.9%, 6.1%, and 6.7%, respectively. Therefore, by increasing the D_3 , the internal flow noise of the MCP can be controlled to some extent.

5. CONCLUSION

The influence of dynamic and static disturbances on the flow and vibration and noise characteristics of a MCP is investigated using the D_3 as a variable.

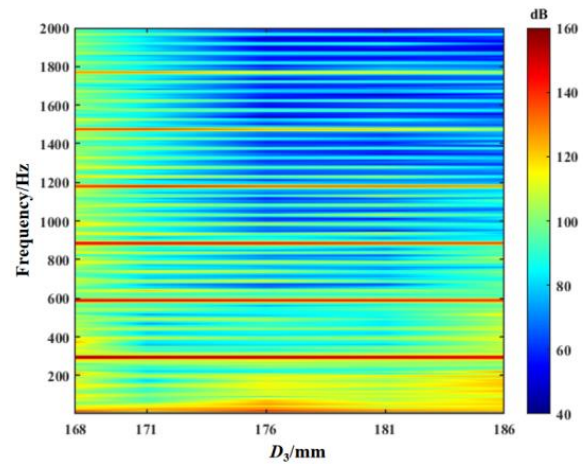


Fig. 17 Broadband spectrum of sound pressure at the outlet measurement points for different base circle diameter.

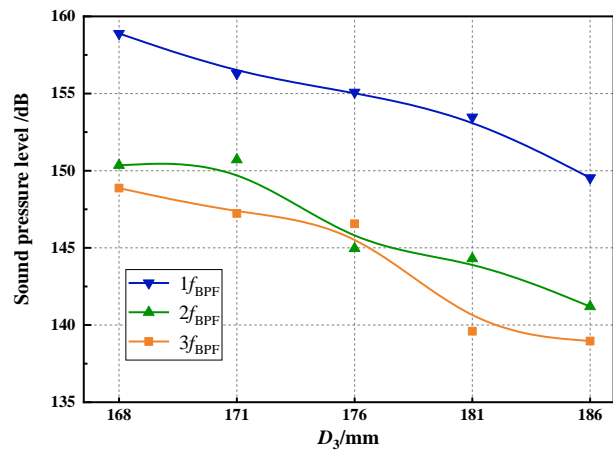


Fig. 18 Sound pressure level of each characteristic frequency with different base circle diameters

(1) The changes in D_3 have little effect on the hydraulic performance of the MCP; the maximum change rate of the head is not more than 1.6%, and that of the MCP efficiency is not more than 2%. As D_3 increases, the velocity gradient inside the volute decreases, the flow pattern becomes increasingly uniform, and the characteristic frequency distribution of the discharge pressure pulsation remains unchanged, but its amplitude decreases.

(2) As D_3 changes, the main frequency of the excitation-induced vibration on the inner surface of the volute coincides with each characteristic frequency. The main frequency is located at $1f_{BPF}$, and the harmonic frequency is located at $2f_{BPF}$, and $3f_{BPF}$. The amplitude of the entire vibration frequency band decreases, as D_3 increases. When D_3 increases from 168 mm to 186 mm, the total vibration levels at the measurement points for the MCP inlet flange, outlet flange, and base decrease by 8.3%, 7.9%, and 12.3%, respectively.

(3) With the increase in D_3 , the characteristic frequency of the SPL at the outlet of the MCP flow noise

changes, and the SPL of the flow noise at each characteristic frequency gradually decreases, indicating that the increase in D_3 appropriately has a certain inhibiting effect on the vibration and noise of the MCP.

ACKNOWLEDGEMENTS

This work was supported by the National Key Research and Development Program of China (No. 2019YFC0312400 and 2019YFC0312404), the National Natural Science Foundation of China (No. 51879122, 51579117 and 51779106). One of the authors (Zhiming Cheng) is grateful for the support received from the China Scholarship Council (CSC).

CONFLICT OF INTEREST

The authors declare that they have no competing interests.

AUTHORS CONTRIBUTION

Z. Cheng: wrote the first version of the manuscript; contribute to the design and simulation; contributed to answering comments. Q. Ma: supervision; review and editing; contributed to answering comments. H. Liu: supervision; contributed to design and simulation; review and editing. L. Dong: methodology; supervision. Q. Pan: validation; review and editing.

REFERENCES

- Arndt, N., Acosta, A., Brennen, C., & Caughey, T. (1989). Rotor-stator interaction in a diffuser pump. *Journal of Turbomachinery*, 111(3), 213-221. <https://doi.org/10.1115/1.3262258>
- Atif, A., Benmansour, S., Bois, G., & Dupont, P. (2011). Numerical and experimental comparison of the vaned diffuser interaction inside the impeller velocity field of a centrifugal pump. *Science China Technological Sciences*, 54(2), 286-294. <https://doi.org/10.1007/s11431-010-4260-5>
- Cao, W., Jia, Z., Zhao, Z., & Zhou, L. (2022). Validation and simulation of cavitation flow in a centrifugal pump by filter-based turbulence model. *Engineering Applications of Computational Fluid Mechanics*, 16(1), 1724-1738. <https://doi.org/10.1080/19942060.2022.2111363>
- Chalghoum, I., Elaoud, S., Kanfoudi, H., & Akrouf, M. (2018). The effects of the rotor-stator interaction on unsteady pressure pulsation and radial force in a centrifugal pump. *Journal of Hydrodynamics*, 30(4), 672-681. <https://doi.org/10.1007/s42241-018-0073-y>
- Chan, W. K., Hu, W., & Wong, Y. W. (2007). Effects of tongue position and base circle diameter on the performance of a centrifugal blood pump. *Artificial Organs*, 31(8), 639-645. <https://doi.org/10.1111/j.1525-1594.2007.00430.x>
- Cheng, Z., Liu, H., Wang, K., Tan, M., Sun, X., & Shen, D. (2022). Experimental study on unbalanced response characteristics of the impeller of mixed transport pump in deep-sea mining. *Proceedings of the Institution of Mechanical Engineers, Part C: Journal of Mechanical Engineering Science*, 237(6), 1279-1290. <https://doi.org/10.1177/09544062221127125>
- Chu, S., Dong, R., & Katz, J. (1995). Relationship between unsteady flow, pressure fluctuations, and noise in a centrifugal pump-part B: effects of blade-tongue interactions. *Journal of Fluids Engineering*, 117(1), 30-35. <https://doi.org/10.1115/1.2816814>
- Croba, D., & Kueny, J. (1996). Numerical calculation of 2D, unsteady flow in centrifugal pumps: impeller and volute interaction. *International Journal for Numerical Methods in Fluids*, 22(6), 467-481. [https://doi.org/10.1002/\(SICI\)1097-0363\(19960330\)22:6<467::AID-FLD324>3.0.CO;2-O](https://doi.org/10.1002/(SICI)1097-0363(19960330)22:6<467::AID-FLD324>3.0.CO;2-O)
- Dong, L., Zhao, Y., Liu, H., Dai, C., Vladimirovich, G., & Wang, Y. (2018). The effect of front streamline wrapping angle variation in a super-low specific speed centrifugal pump. *Proceedings of the Institution of Mechanical Engineers, Part C: Journal of Mechanical Engineering Science*, 232(23), 4301-4311. <https://doi.org/10.1177/0954406218772605>
- Dong, X., & Dou, H. (2021). Effects of Bionic Volute Tongue Bioinspired by Leading Edge of Owl Wing and Its Installation Angle on Performance of Multi-Blade Centrifugal Fan. *Journal of Applied Fluid Mechanics*, 14(4), 1031-1043. <https://doi.org/10.47176/jafm.14.04.31987>
- Guo, C., Gao, M., Lu, D., & Guan, H. (2018). Experimental study on radiation noise frequency characteristics of a centrifugal pump with various rotational speeds. *Applied Sciences*, 8(5), 796. <https://doi.org/10.3390/app8050796>
- Iversen, H., Rolling, R., & Carlson, J. (1960). Volute pressure distribution, radial force on the impeller, and volute mixing losses of a radial flow centrifugal pump. *Journal of Engineering for Turbines & Power*, 82(2), 136-143. <https://doi.org/10.1115/1.3672734>
- Jia, X., Chu, Q., Zhang, L., & Zhu, Z. (2022). Experimental study on operational stability of centrifugal pumps of varying impeller types based on external characteristic, pressure pulsation and vibration characteristic tests. *Frontiers in Energy Research*, 10. <https://doi.org/10.3389/fenrg.2022.866037>
- Kuang, R., Zhang, Z., Wang, S., & Chen, X. (2021). Effect of hub inclination angle on internal and external characteristics of centrifugal pump impellers. *AIP Advances*, 11(2), 1-10. <https://doi.org/10.1063/5.0038109>
- Kunz, D., & Newkirk, M. (2009). A generalized dynamic balancing procedure for the AH-64 tail rotor. *Journal of Sound and Vibration*, 326(1-2), 353-366. <https://doi.org/10.1016/j.jsv.2009.04.043>
- Liu, H., Ma, Q., Li, Y., & Wang, Kai. (2020). Vibration

- control of a marine centrifugal pump using floating raft isolation system. *Journal of Low Frequency Noise, Vibration & Active Control*, 39(2), 382-392. <https://doi.org/10.1177/1461348419843024>
- Ma, C., Hong, Z., Zhang, H., & Wu, X. (2021). Aerodynamic excitation and vibration analysis of centrifugal compressor impeller under dynamic and static interference. *Transaction of Beijing Institute of Technology*, 41(9), 935-942. <https://doi.org/10.15918/j.tbit1001-0645.2020.109>
- Mohamed, H., Mostafa, M., Ramy, E., & Mahmoud, A. (2019). Numerical simulation of centrifugal pump and effect of impeller geometry on its performance. *Engineering and Applied Sciences*, 4(2), 21-29. <https://doi.org/10.11648/j.eas.20190402.11>
- Ren, K., Shuai, Z., Wang, X., Jian, J., Yu, T., Dong, L., Li, W., & Jiang, C. (2022). Aerodynamic noise prediction of a high-speed centrifugal fan considering impeller-eccentric effect. *Engineering Applications of Computational Fluid Mechanics*, 16(1), 780-803. <https://doi.org/10.1080/19942060.2022.2042392>
- Shadab, M., Karimipour, M., Najafi, A., Raydar, R., & Nourbakhsh, S. (2022). Effect of impeller shroud trimming on the hydraulic performance of centrifugal pumps with low and medium specific speeds. *Engineering Applications of Computational Fluid Mechanics*, 16(1), 514-535. <https://doi.org/10.1080/19942060.2021.2016492>
- Spence, R., & Amaral-Teixeira J. (2009). A CFD parametric study of geometrical variations on the pressure pulsations and performance characteristics of a centrifugal pump. *Computers and Fluids*, 38(6), 1243-1257. <https://doi.org/10.1016/j.compfluid.2008.11.013>
- Spence, K., Lin, B., & Hung, C. (2008). Novel design of centrifugal pump impellers using generated machining method and CFD. *Engineering Applications of Computational Fluid Mechanics*, 2(2), 195-207.
- Yuan, S., Ni, Y., Pan, Z., & Yuan, J. (2009). Unsteady turbulent simulation and pressure fluctuation analysis for centrifugal pumps. *Chinese Journal of Mechanical Engineering*, 22(1), 64-69. <https://doi.org/10.3901/CJME.2009.01.064>
- Zhou, Y., Yin, Y., & Zhang, Q. (2013). Active control of repetitive impulsive noise in a non-minimum phase system using an optimal iterative learning control algorithm. *Journal of Sound and Vibration*, 332(18), 4089-4102. <https://doi.org/10.1016/j.jsv.2013.03.004>